

Stellar kinematics and populations out to 1.5 effective radius in the elliptical galaxy NGC4636

S. B. Pu^{1,2,3} * and Z. Han^{1,3}

¹ National Astronomical Observatory/Yunnan Observatory, the Chinese Academy of Sciences, Kunming 650011, China

² Graduate University of Chinese Academy of Sciences, Beijing 100049, China

³ Key Laboratory of the Structure and Evolution of Celestial Objects, Chinese Academy of Sciences, Kunming 650011, China

Abstract We present high quality long slit spectra along the major and minor axes out to 1.5 effective radius (R_e) of the massive galaxy NGC4636 taken by Hobby-Eberly Telescope (HET). Using Fourier Correlation Quotient (FCQ) method, we measured the stellar line-of-sight velocity distribution along the axes. Furthermore, six Lick/IDS indices ($H\beta$, Mgb , Fe_{5015} , Fe_{5270} , Fe_{5335} , Fe_{5406}) are derived from the clean spectrum. By comparing the measured absorption line strengths with the predictions of Simple Stellar Populations (SSP) models, we derived ages, total metallicity and α abundance profiles of the galaxy. This galaxy presents old and $[\alpha/Fe]$ over abundant stellar populations. Indeed, using the SSP model, we obtained the broadband color profiles. The theoretical colors match well with the measured colors and present red sharp peaks at the galaxy center. The sharp peaks of the colors are mainly shaped by the high metallicity in the galaxy center. Interestingly, the galaxy has steep negative metallicity gradients, but trend flattens outwards. This result likely suggests that the center and outer regions of the galaxy formed through different formation process.

Key words: galaxy:elliptical and lenticular-galaxy:abundances -galaxy: kinematic and dynamics -galaxy:individual (NGC4636)

1 INTRODUCTION

The formation and evolution of massive, early-type galaxies constitutes a long-standing and crucial problem in cosmology (Sánchez-Blázquez et al. 2007). According to the classic monolithic-collapse model for the formation and evolution of early-type galaxies (Tinsley 1972; Larson 1975; Tantaló et al. 1996), the early-type galaxies formed most of their stars during a single short and highly efficient star formation event in the early universe. This model is strongly supported by the extremely small scatter of the observed color magnitude relation of elliptical galaxies. This uniformity of stellar populations in ellipticals is also supported by the Fundamental Plane (Dressler et al. 1987; Djorgovski & Davis 1987; Bender et al. 1992; Saglia et al. 1993). Moreover, the tightness of the $Mg - \sigma$ relation for massive elliptical galaxies observed in the local universe (Bender et al. 1993; Sánchez-Blázquez et al. 2007) but holding up to the intermediate redshift $z \approx 1$ (Ziegler & Bender 1997; Bender et al. 1998) requires a picture of a short, and highly efficient star formation process at high redshift and passive evolution since then.

* e-mail:pushibi@hotmail.com

In contrast, according to the hierarchical merging scenario (White & Rees 1978; Kauffmann et al. 1993), the massive early-type galaxies are expected to have formed through multiple mergers and the accretion of smaller objects over an extended period (White & Frenk 1991; Somerville & Primack 1999; De Lucia et al. 2006). This formation scenario has been observationally confirmed; COMBO-17 and DEEP2 surveys show that the number density of red galaxies has increased since redshift $z=1$ (Bell et al. 2004; Faber et al. 2007). Furthermore, giant galaxies show boxy isophotes and anisotropic dynamics, and more massive galaxies are more radio-loud, more strong X-ray emitters, more frequently disturbed. On the contrary, normal and low luminosity elliptical galaxies rotate rapidly, are nearly isotropic, show diskly distorted isophotes and cuspy inner profiles. The properties of the former can be explained in dissipationless mergers, while the latter are recovered successfully with dissipational mergers (Nieto & Bender 1989; Bender et al. 1989; Bender & Surma 1992; Barnes 1992; Mehlert et al. 1998). Recently, Kuntschner (2000); Thomas et al. (2005); Collobert et al. (2006); Bernardi et al. (2006); Clemens et al. (2006); Rogers et al. (2010) showed that early-type galaxies in low density and in high density environments might exhibit different formation ages, and Lisker et al. (2008); Sánchez-Blázquez et al. (2009); Matković et al. (2009) found evidence that lower mass galaxies have more extended star formation histories.

Radial profiles of the kinematics, colors, ages and metallicities of the stellar populations are the efficient tools to study galaxy formation scenarios. In standard closed-box models of chemical enrichment, the metallicity is a function of the yield and of how much gas has been locked after star formation has ceased (Tinsley 1980). Therefore, the metallicity strongly depends on the dynamical parameters. For instance, for galaxies formed via a monolithic-collapse, stars formed in all regions during the collapse and remain in their orbits with little movement inward, whereas the gas dissipates into the center, being continuously enriched by the evolving stars. Therefore, stars formed in the center are predicted to be more metal rich than those in the outer regions. So far the galaxies should have steep radial metallicity gradients (Larson 1976; Thomas 1999; Sánchez-Blázquez et al. 2007). On the other hand, major mergers, which come along with hierarchical merging, will dilute stellar population gradients (White 1980; Kobayashi 2004; Hopkins et al. 2009; Tortora et al. 2011). Therefore, more flat population gradients are expected within this picture. Accordingly, the observation of stellar population gradients and their connection to dynamical parameters can give crucial insight into the formation paths of individual galaxies.

This work is aiming to deeply investigate the stellar kinematics and populations of the massive galaxy NGC4636. NGC4636 is an E/S0 galaxy, located at about 2.8Mpc southeast from the Virgo center and 14.7 Mpc [$(m - M)_0 = 30.83 \pm 0.13$] from us. Effective radius, ellipticity, and position angle of major axis of NGC4636 are $R_e = 88.5''$, $\epsilon_e = 0.256$, and $PA = 150^\circ$, respectively (Tonry et al. 2001; Rampazzo et al. 2005; Kim et al. 2006; Schuberth et al. 2006). NGC4636 is considered to be a major member of a small group falling into the Virgo center (Nolthenius 1993). Although, it is relatively less luminous ($M_v = -21.7$ mag,) among the gEs in Virgo, but NGC4636 shows several interesting features. For instance, NGC4636 is found to be very bright in X-rays ($L_X \sim 10^{41}$ ergs s^{-1}), with unusual feature in the hot interstellar medium (ISM) (O'Sullivan et al. 2005; Kim et al. 2006; Posson-Brown et al. 2009). The galaxy NGC4636, has boxy isophotes (Rembold et al. 2002) and does not show rotation both along major and minor axes (Davies et al. 1993; Bender et al. 1994; Rampazzo et al. 2005). Indeed, NGC4636 is one of the best targets for studying kinematics of globular clusters since it has an anomalously large number of GCs (Dirsch et al. 2005; Chakrabarty & Raychaudhury 2008; Park et al. 2010; Lee et al. 2010).

There is a number of works which focus on the study of kinematic profiles, line strength indices and stellar population parameters in NGC4636 (Davies et al. 1993; Bender et al. 1994; Tantalo et al. 1998; Rampazzo et al. 2005; Annibali et al. 2006; Li et al. 2007). However, the previous measurements are concentrated within $R_e/2$ of galaxies. From a comparison of the stellar parameters within $R_e/8$ with these within $R_e/2$ of some early-type galaxies sample, Davies et al. (1993); Trager et al. (2000); Denicoló et al. (2005) found that the elliptical galaxies present slightly negative metallicity gradients from the centers to the outer regions and the ages are likely to increase slightly outwards. The same trends were detected by Fisher et al. (1995). But still only 1/3 of the star mass is contained within $R_e/2$.

Table 1 Log of spectroscopic observation, MJ = major axis; MN = minor axis; SKY= sky spectrum.

Date	Objects	Position	Seeing(FWHM)
2008 Apr 04	NGC4636	MJ1, SKY1	2.57
2008 Apr 06		MJ2,3, SKY2	1.49
2008 Apr 09		MJ4,5, SKY3	1.64
2008 May 01		MN1,2, SKY4	1.92

^a The exposure time for each slit is 900 seconds.

^b Position angles of major and minor axes of NGC4636 are 150° and 60° respectively.

In this work, we obtained deep long slit spectra of the local galaxy NGC4636 outer to 1.5 R_e , aiming to study the stellar populations and kinematics out to larger radius and give crucial insight into the formation paths of galaxy.

The paper is organized as follows. In Sect. 2 we describe the observations (Sect. 2.1) and the data reduction (Sect. 2.2). In Sect. 3 we present the kinematics (Sect. 3.1) and the line strength measurements (Sect. 3.2). We analyze the Lick indices and derive ages, metallicities, and α/Fe ratios, present the colors and mass-to-light ratios and briefly describe the models and the method used in Sect. 4. A summary of this work is presented in Sect. 5. The full data table of kinematics and Lick/IDS indices are shown in Sect.6.

2 OBSERVATION AND DATA REDUCTION

2.1 Observation

Long-slit spectra along major and minor axis of NGC4636 were collected during the period of April to May in 2008 using the HET in service mode and the Low-Resolution Spectrograph (LRS) with the E2 grism (Hill et al. 1998). In order to detect the galaxy outer regions, the center of the galaxy was moved towards one end of the slit. The slit width was 3 arcsec, giving an instrumental broadening of $\sigma_{inst} = 120$ km/s and covering the wavelength range from 4790 to 5850 (Å). The exposure time of each slit was 900 sec. Moreover, 900 sec exposures of blank sky regions were taken at regular intervals. The seeing ranged from 1.49 to 2.57 arcsec. The resulting summed spectra probe regions out to nearly 1.5 R_e of NGC4636. In addition, calibration frames (biases, dome flats and the Ne and Cd lamps) were taken. Table 1 shows the logs of the spectroscopic observations.

2.2 Data Reduction

The data reduction used the MIDAS package provided by ESO. The pre-process of data reduction was done following Bender et al. (1994). The raw spectra were bias subtracted, and divided by the flat-fields. The cosmic rays were removed with a $\kappa - \sigma$ clipping procedure. The wavelength calibration was performed using 9 to 11 strong Ne and Cd emission lines and a third order polynomial. The achieved accuracy of the wavelength calibration is always better than 0.6 Å (rms). The science spectra were rebinned to a logarithmic wavelength scale.

The step of sky subtraction required particular care to minimize systematic effects on the measured kinematics and line strengths in the outer regions of our galaxies. More details can be seen in Saglia et al. (2010, Fig. 2) and Pu et al. (2010, Fig.1;Fig2). Here, We briefly describe the calibration of the atmospheric sky level procedure. At the beginning, we selected the spectra of galaxy where a sky spectrum with a uniform slit illumination was available, and almost photometric conditions were achieved, yielding the largest galaxy counts per pixel. To correct for the inhomogeneous slit illumination, we produced a 4th to 6th order polynomial model of the sky spectra for each column in spatial direction and subtracted it from the selected galaxy frames, obtaining a reference science frames G_r . We

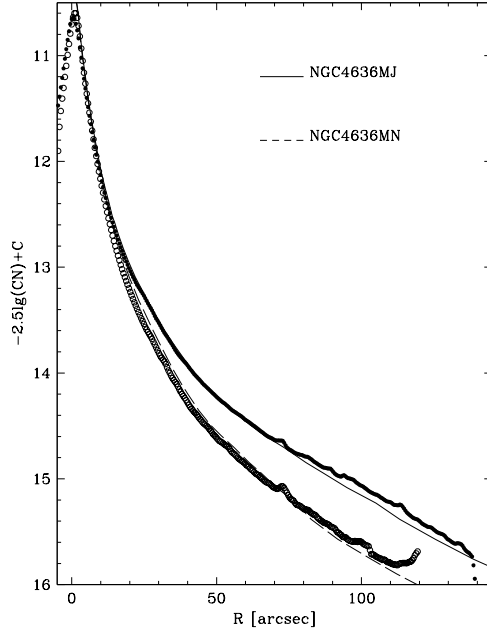


Fig. 1 The comparison between the broadband surface brightness profiles (lines) and the ones derived from our summed spectra (dots) for NGC4636. The solid and open dots indicate the profiles measured from the summed spectrum along the major and minor axes respectively. The solid and dashed lines present the V band photometry data taken from Kormendy et al. (2009).

computed the fractional residuals between the scaled and the reference slit profiles

$$R(r) = \left| 1 - \frac{f_i^G * \langle G_r \rangle}{\langle (G_i - f_i^S * SKY_i) \rangle} \right|. \quad (1)$$

and minimized it (see below). Here f_i^S is the scaling factor of the noise-free (i.e. the polynomial model) sky frame taken after the galaxy frame G_i , when available, or the average of the most uniform sky frames when not. The symbol $\langle \rangle$ indicates the average in the wavelength direction and $R(r)$ is a function of the position r along the slit. Moreover, f_r^G is a scaling factor that takes into account the different atmospheric transmissions. We determined f_i^G and f_i^S iteratively such to minimize R , which in an ideal situation should be zero at every radii. Finally, we computed the resulting total galaxy frame G_{tot} as:

$$G_{tot} = G_r + \Sigma_i (G_i - f_i^S * SKY_i) / f_i^G. \quad (2)$$

In practice, due to the non-uniformity of the slit illumination function the function $R(r)$ is not always zero, but through the summing in Eq. 2 the differences should average out. We can test the quality of the calibration by comparing the profile $\langle G_{tot} \rangle$ with available broadband photometry. Figure 1 shows the comparison between the summed shifted slit profiles and the broadband photometry of the galaxy. The solid and open dots indicate the counts number profiles measured from the summed spectrum of major and minor axes respectively. The solid and dashed lines present the V band photometry data taken from Kormendy et al. (2009). The plot confirm that the summed spectrum agrees well with the broadband photometry out to large radius.

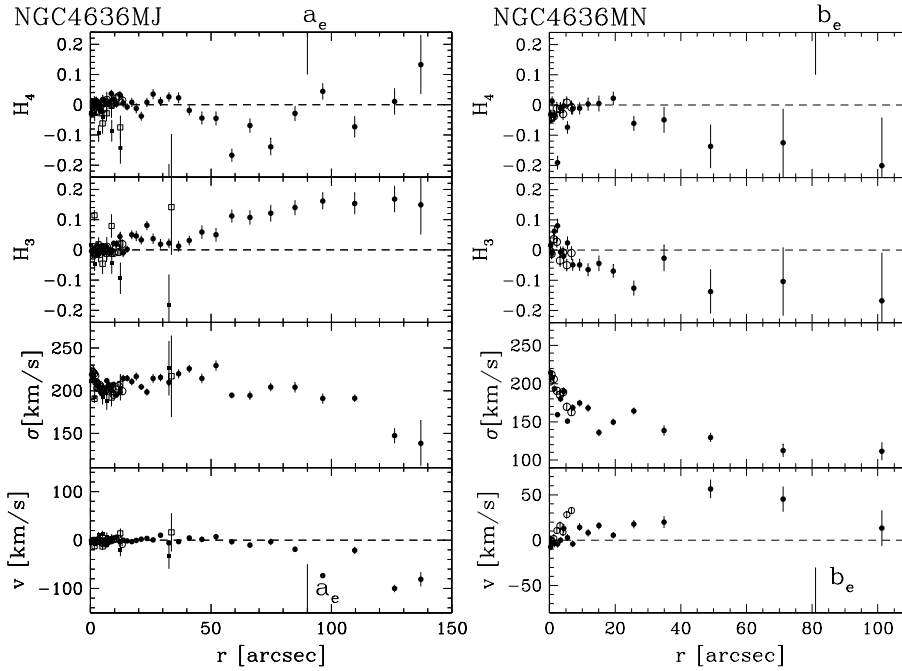


Fig. 2 The stellar kinematics profiles along the major and minor axes of NGC4636. From bottom to top in each panel we show: (1) Rotation velocity, (2) Velocity dispersion, (3) and (4) Gauss-Hermite parameters H_3 and H_4 . The profiles are folded with respect to the nucleus of the galaxy, filled and open symbols stand for different sides of the galaxy. The squares show the data published in Bender et al. (1994).

In addition, we also need to correct the anamorphic distortion of the LRS, remove sky emission line spectrum and remove the continuum spectra. The procedures are described in details in Pu et al. (2010).

3 KINEMATIC AND LICK/IDS INDICES PROFILES

3.1 Kinematics Profiles

We extracted the line-of-sight velocity distributions (LOSVDs) and kinematic parameters from the continuum-removed spectra that rebinned radially to obtain almost constant signal-to-noise ratio, using the Fourier Correlation Quotient (FCQ) method (Bender 1990) with the implementation described in Saglia et al. (2010) that allows for the presence of emission lines. The stellar spectra library of Vazdekis (1999) is used as the templates aiming to minimize the mismatching. This library contains about a thousand synthetic single-stellar-population spectra covering the wavelength range from 4800 to 5470 Å with a resolution of 1.8 Å. We used the library with ages of 1.00 to 17.78 Gyr and metallicities from -1.68 to 0.2. We first set all of the library spectra to the resolution of our galaxy spectra and find the best fitting template for each radial bin according to the lowest RMS value of the residual (reaching typically 1% of the initial flux). If emission lines are detected, Gaussians are fitted to the residuals above the best-fit template and subtracted from the galaxy spectrum to derive cleaned spectra. The kinematic fit is then redone using these cleaned spectra. We do not detect emission in the spectra of NGC4636.

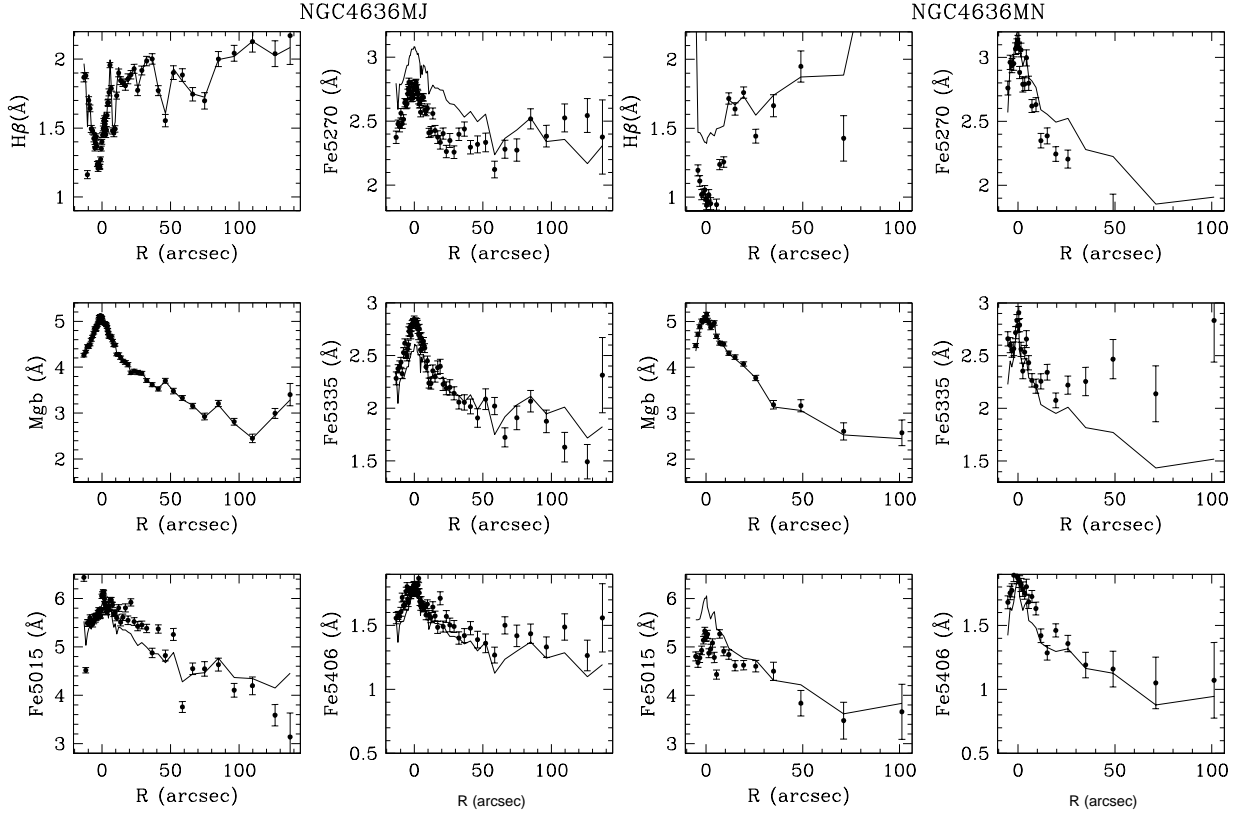


Fig. 3 The line-strength indices along the major and minor axis. The names of the indices are labeled and the galaxies' names are also noted. The solid lines show the model (TMB03) predicted line strength profiles along the axes.

The Fig. 2 presents the kinematics along the major and minor axes in NGC4636. In this figure we show the rotational velocity, the velocity dispersion and the Gauss-Hermite parameters H_3 and H_4 . The filled symbols show the kinematic profiles on south-east (SE) side along the major axis and north-east (NE) side along the minor axis. The reference data taken from Bender et al. (1994) are also dotted in squares in the plot. As it can be seen from the figures, agreement is generally good. The $a_e = R_e \cdot \epsilon^{-1/2}$ and $b_e = R_e \cdot \epsilon^{1/2}$ are labeled, where the R_e is the effective radius and the ϵ is the apparent axial ratio. The kinematics data extend to 140 arcsec along major axis and 105 along minor axis from the galaxy center. Further extend out than the previous work of Bender et al. (1994); Davies et al. (1993); Rampazzo et al. (2005). The kinematic profiles present no rotation both along major and minor axes. The velocity dispersion show flat gradients inside 100 arcsec and become steep along major axis. The measured stellar kinematics with errors table is presented in Table.2 in Appendix.

3.2 Lick/IDS indices Profiles

In this section, we describe the measurement of six Lick/IDS indices ($H\beta$, Mgb , Fe_{5015} , Fe_{5270} , Fe_{5335} , Fe_{5406}), which defined by Trager et al. (1998). The line strength indices have been measured from the cleaned spectra along the major and minor axis. Before measuring the indices, our spectra were degraded to the resolution of Lick/IDS systems. We then corrected the

indices for the velocity dispersion using template stars and the value for σ derived in the previous section. Finally, the observational data need to be corrected to the Lick/IDS system. To do this we observed 5 stars from the Lick/IDS library using the same instrumental configuration used for the science objects and derived the offsets between our data and the Lick/IDS system. The comparison of our data with the Lick standard systems can be found in Pu et al. (2010, Fig. 4). The data are in good agreement with the Lick/IDS systems, as found in Saglia et al. (2010) using a larger set of Lick standards observed with LRS and HET at a better resolution. So far, the deviation between our measurements and the Lick system can be ignored, but we take into account the RMS of the calibration lines into the final error budget, by adding it in quadrature to the statistical error of each index. Fig.3 shows the six line strength indices profiles along the major and minor axes of the galaxy. The names and positions are labeled in the figure. The dots present the measured lick/IDS and the solid lines show the SSP models predictions, they will be discussed in the following sections. The full table of six Lick/IDS indices is presented in Table. 3 in the Appendix. The galaxy presents positive gradients of $H\beta$ index both along major axis and minor axis, very similar to profiles in another galaxies discovered in previous work (Davies et al. 1993; Sánchez-Blázquez et al. 2007; Pu et al. 2010). We also measured the indices Mg_1 and Mg_2 , but we do not use them in this work since these two indices are very sensitive to the anamorphic distortion.

4 STELLAR POPULATIONS

In this section, we derive the age, total metallicity and element abundance gradients along the major and minor axes by comparing the measured line indices with simple stellar population models (TMB03). The details of this model can be seen from Thomas et al. (2003, 2005). Here, we give a brief description of this model: The TMB03 models cover ages between 1 and 15 Gyr, metallicities between 1/200 and 3.5 solar. Furthermore, the models take into account the effects on the Lick indices by the variation of α abundance, hence, give Lick indices of simple stellar populations not only as the function of age and metallicity, but also as the function of the α/Fe ratio.

In this work, we do not adopt the traditional and effective method of studying stellar population properties which uses diagrams of different pairs of Lick indices (Thomas et al. 2005). The method selects the $H\beta$ versus $[MgFe]'$ pair diagram to break the age-metallicity degeneracy, where, $[MgFe]'$ = $\sqrt{Mgb[0.72Fe5270 + 0.28Fe5335]}$, because $H\beta$ is sensitive to warm turnoff stars and $[MgFe]'$ index is considered as the best detector of metallicity since it does not depend on abundance ratio variations. Following Saglia et al. (2010) and Pu et al. (2010), we use the simple χ^2 minimization method. χ^2 method fits all of $H\beta$, Mgb , $Fe5270$, $Fe5335$ and other available indices at the same time, the best resolution is bound to break the age-metallicity degeneracy. The tests for Coma galaxies done by Thomas et al. (2011) show that the results which derived using new method were better than the results obtained using the traditional method. The χ^2 is give by:

$$\chi^2 = \sum_{index[i]} \frac{(index_{i[obs]} - index_{i[mod]})^2}{(\sigma_{i[obs]})^2} \quad (3)$$

where $index_{i[obs]}$ and $index_{i[mod]}$ represent the i^{th} observational indices and model indices respectively, $\sigma_{i[obs]}$ is the observational uncertainty of i^{th} indices. We can derive the best fitting age, metallicity and α/Fe by finding the minimum χ^2 of all selected lines indices to the SSP models. The $H\beta$, Mgb , Fe_{5015} , Fe_{5270} , Fe_{5335} and Fe_{5406} are used as the indicators. Moreover, we interpolated the tabulated indices of TMB03 on steps of 0.1 Gyr in age, 0.02 in metallicity and 0.05 in α/Fe aiming to improve the precision of the stellar properties using the χ^2 minimization method.

Fig. 4 presents the model predicted age, metallicity, element abundance, colors, mass-to-light ratios, and resulting χ^2 . From the top left panel to the bottom left panel, the age, total metallicity $[Z/H]$ and α/Fe ratio are shown. The galaxy presents α overabundant from the galaxy center to the outer parts. The total metallicity profile shows a steep negative gradients with $\Delta[Z/H]/\Delta \log(r) = -0.333 \pm 0.022$ inner R_e and become flat outwards. The average age, metallicity and α/Fe inside $1/16 R_e$ are 9.96

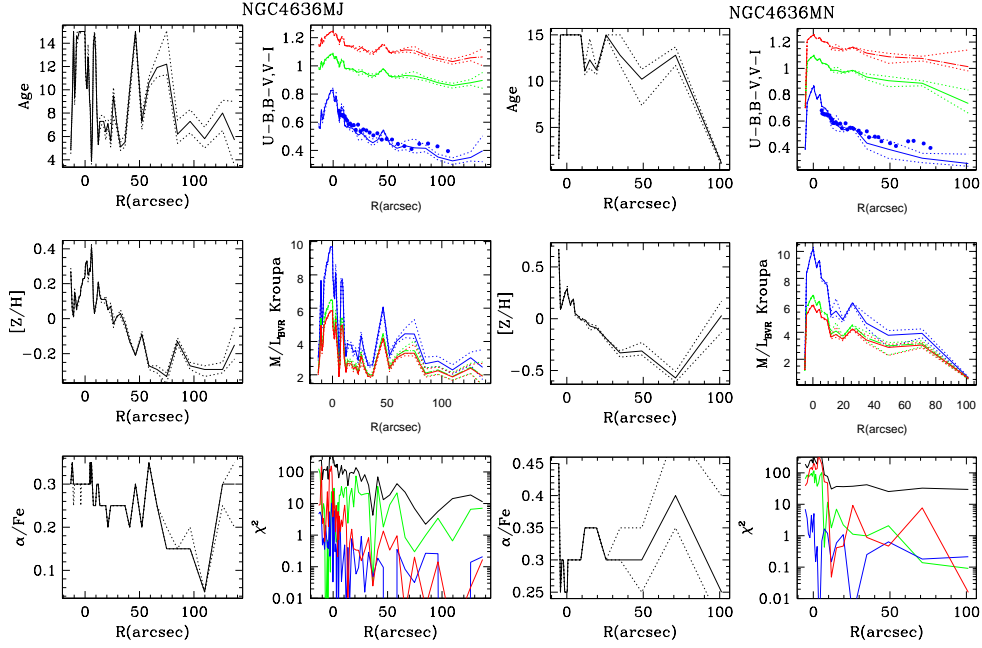


Fig. 4 The best fitting SSP equivalent age, metallicity and element abundance ratio are shown in the left in each plot. The right top of each plot shows the Johnson broadband U-B, B-V, V-I colors profiles, the blue and green solid lines stand for U-B and B-V color respectively; the red solid lines indicate the V-I color. The measured U-B color taken from Peletier et al. (1990) are dotted with blue solid symbols. The M/L_{BVI} are shown in the mid of the right columns, the blue, green and red solid lines indicate the M/L in the B, V and I band respectively; the minimized χ^2 of selected line strengths are presented in the bottom panel on the right, red, blue and green lines present the minimized χ^2 of $H\beta$, Mgb and Fe_{5270} respectively; while the black lines show the total minimized χ^2 .

± 1.83 Gyr, 0.302 ± 0.08 and 0.325 ± 0.025 . They are comparable to the results of age = 9.918 ± 0.458 derived by Sánchez-Blázquez et al. (2006) using the $H\beta$ versus $[Mgb]$ pair diagram and the age = 8.18 ± 0.063 in Proctor & Sansom (2002). The model predicted lines strength profiles are shown in Fig. 3 with solid lines. As it can be seen from Fig. 3, in generally, theoretical line strength indices match well with the measured parameters in the inner regions of the galaxies except Fe_{5270} due to this indices be contaminated by some unknown sky lines and we set its weight to zero. In addition, we also calculate the Johnson broadband U-B, U-V, B-V, V-R, V-I, V-K, J-K, J-H, H-K color and M/L ratio in B, V, R, I, J, H, and K bands profiles using the Kroupa initial mass function (Kroupa 1995) with the help of the SSP models (Maraston 1998). For a clear presentation in the figures, we only show the U-B, B-V and V-I color and the mass to light ratios in B, V, I band in this papers. On the top right panels in Fig. 4, the blue and green solid lines stand for U-B and B-V color respectively; the red lines indicate the V-I color. The measured U-B color [taken from (Peletier et al. 1990)] are also over plotted with solid blue dots. As it can be seen from the plot, the model predicted color profiles agree well with the measured colors. Indeed, the colors present steep negative gradients and sharp peaks, this feature mainly shaped by the metallicity profile. The middle right panel of Fig.4 shows the theoretical M/L ratio in B, V, I bands; the blue, green and red lines display the M/L ratios in B, V and I colors respectively; The minimized χ^2 of selected line strength are presented in the bottom panel on right, red, blue and green lines present the

minimize χ^2 of $H\beta$, Mgb and Fe_{5270} respectively; while the black lines show the total minimized χ^2 . The large values of χ^2 along major axis are mainly driven by the Fe_{5270} .

5 SUMARRY AND DISCUSSION

In this work, we measured the accurate kinematic profiles extending out to 1.5 R_e along the major and minor axis for the giant elliptical galaxy NGC4636. Indeed, six Lick line indices ($H\beta$, Mgb , Fe_{5015} , Fe_{5270} , Fe_{5335} , Fe_{5406}) defined by Burstein et al. (1984); Worthey et al. (1994); Trager et al. (1998) of NGC4636 are also derived. By comparing the measured Lick/IDS with the SSP model predictions, we derived the stellar population parameters, the M/L ratios and the broadband colors of our galaxies. We found the galaxy NGC4636 has high metallicities in the galaxy center and presents steep negative metallicity gradients. The galaxy is α overabundant and do not present significant gradients of α abundances along the axes. The galaxy have sharp red peaks at the center which be mainly shaped by the metallicity (Maraston 1998). The model predicted colors agree well with the measured color profiles.

According to the simple element enrichment scenario, the α elements are mainly delivered by Type II supernovae explosions of massive progenitor stars, and a substantial fraction of Fe peak elements come from the delayed exploding Type Ia supernovae (Nomoto et al. 1984; Thielemann et al. 1996). Thus the α/Fe can be used as an indicator to constrain the formation timescale of stars. Hence the flat profile of α/Fe ratio in our galaxy likely suggests that there is no radial variation of star formation time scales. The radial metallicity and lines strength gradients give one of the most stringent constraints on the galaxy formation (Sánchez-Blázquez et al. 2006; Tortora et al. 2011). The galaxies that form monolithically have steeper gradients and the galaxies that undergo major mergers have shallower gradients. The mean metallicity gradients for non-merger and merger galaxies derived by theoretical simulation in Kobayashi (2004) are $\Delta[Z/H]/\Delta \log(r) \sim -0.30 \pm 0.2$ and -0.22 ± 0.2 , respectively. The author found that the galaxies with gradients steeper than -0.35 are all non-major merger galaxies. The gradients inside R_e of NGC4636 is $\Delta[Z/H]/\Delta \log(r) = -0.333 \pm 0.022$; while the gradients of NGC4636 becomes flat outer R_e . Accordingly, this is a weak indication that the center and the out regions of NGC4636 are formed through different formation process. Indeed, it is worthwhile to observe the Lick/IDS in further out regions with newly developed observing technique as done by Weijmans et al. (2009). And it will give us a new insight on the formation of the elliptical galaxies.

In the forthcoming works, we plan to further investigate the dynamical structure and orbit distribution of NGC4636, to investigate further constraints on the formation process of the galaxy.

Acknowledgements We specially thank the McDonald Observatory for performing the observations with Hobby-Eberly Telescope (HET) in service mode. The HET is a joint project of the University of Texas at Austin, the Pennsylvania State University, Stanford University, Ludwig-Maximilians-Universität München, and Georg-August-Universität Göttingen. The HET is named in honor of its principal benefactors, William P. Hobby and Robert E. Eberly.” The Marcario Low Resolution Spectrograph is named for Mike Marcario of High Lonesome Optics who fabricated several optics for the instrument but died before its completion. The LRS is a joint project of the Hobby-Eberly Telescope partnership and the Instituto de Astronomía de la Universidad Nacional Autónoma de México. This work was in part supported by the Chinese National Science Foundation (Grant No. 10821061) and the National Basic Research Program of China (Grant No. 11033008, 2007CB815406). We also gratefully acknowledge the Chinese Academy of Sciences and Max-Planck-Institut für extraterrestrische Physik that partially supported this work. Z.Han thanks the support of the Chinese Academy of Sciences (Grant No. KJXC2-YW-T24). We thank Prof. Bender gave us the HET time to perform the obserations. We are grateful to Dr. R.P.Saglia and J.Thomas for reading the manuscript and useful suggestion. We really appreciate the referee for useful comments that help us to improve the presentation of the results.

References

Annibali, F., Bressan, A., Rampazzo, R., & Zeilinger, W. W. 2006, A&A, 445, 79

- Barnes, J. E. 1992, *ApJ*, 393, 484
- Bell, E. F., Wolf, C., Meisenbeimer, K., et al. 2004, *ApJ*, 608, 752
- Bender, R. 1990, *A&A*, 229, 441
- Bender, R., Burstein, D., & Faber, S. M. 1992, *ApJ*, 399, 462
- Bender, R., Burstein, D., & Faber, S. M. 1993, *ApJ*, 411, 153
- Bender, R., Saglia, R. P., & Gerhard, O. E. 1994, *MNRAS*, 269, 785
- Bender, R., Saglia, R. P., Ziegler, B., et al. 1998, *ApJ*, 493, 529
- Bender, R. & Surma, P. 1992, *A&A*, 258, 250
- Bender, R., Surma, P., Doebereiner, S., Moellenhoff, C., & Madejsky, R. 1989, *A&A*, 217, 35
- Bernardi, M., Nichol, R. C., Sheth, R. K., Miller, C. J., & Brinkmann, J. 2006, *AJ*, 131, 1288
- Burstein, D., Faber, S. M., Gaskell, C. M., & Krumm, N. 1984, *ApJ*, 287, 586
- Chakrabarty, D. & Raychaudhury, S. 2008, *AJ*, 135, 2350
- Clemens, M. S., Bressan, A., Nikolic, B., et al. 2006, *MNRAS*, 370, 702
- Collobert, M., Sarzi, M., Davies, R. L., Kuntscher, H., & Colless, M. 2006, *MNRAS*, 370, 1213
- Davies, R. L., Sadler, E. M., & Peletier, R. F. 1993, *MNRAS*, 262, 650
- De Lucia, G., Springel, V., White, S. D. M., Croton, D., & Kauffmann, G. 2006, *MNRAS*, 366, 499
- Denicoló, G., Terlevich, R., Terlevich, E., Forbes, D. A., & Terlevich, A. 2005, *MNRAS*, 358, 813
- Dirsch, B., Schuberth, Y., & Richtler, T. 2005, *A&A*, 433, 43
- Djorgovski, S. & Davis, M. 1987, *ApJ*, 313, 59
- Dressler, A., Lynden-Bell, D., Burstein, D., et al. 1987, *ApJ*, 313, 42
- Faber, S. M., Willmer, C. N. A., Wolf, C., et al. 2007, *ApJ*, 665, 265
- Fisher, D., Franx, M., & Illigworth, G. 1995, *ApJ*, 448, 119
- Hill, G. J., MacQueen, P. J., Nicklas, H., et al. 1998, in *Bulletin of the American Astronomical Society*, Vol.30, *Bulletin of the American Astronomical Society*, 1262
- Hopkins, P. F., Cox, T. J., Dutta, S. N., et al. 2009, *ApJS*, 181, 135
- Kauffmann, G., White, S. D. M., & Guiderdoni, B. 1993, *MNRAS*, 264, 201
- Kim, E., Kim, D., Fabbiano, G., et al. 2006, *ApJ*, 647, 276
- Kobayashi, C. 2004, *MNRAS*, 347, 740
- Kormendy, J., Fisher, D. B., Cornell, M. E., & Bender, R. 2009, *ApJS*, 182, 216
- Kroupa, P. 1995, *ApJ*, 453, 350
- Kuntschner, H. 2000, *MNRAS*, 315, 184
- Larson, R. B. 1975, *MNRAS*, 173, 671
- Larson, R. B. 1976, *MNRAS*, 176, 31
- Lee, M. G., Park, H. S., Hwang, H. S., et al. 2010, *ApJ*, 709, 1083
- Li, Z., Han, Z., & Zhang, F. 2007, *A&A*, 464, 853
- Lisker, T., Han, Z., & Zhang, F. 2008, *ApJ*, 680, 1042
- Maraston, C. 1998, *MNRAS*, 300, 872
- Matković, A., Guzmán, R., Sánchez-Blázquez, P., et al. 2009, *ApJ*, 691, 1862
- Mehlert, D., Saglia, R. P., Bender, R., Wegner, G. 1998, *A&A*, 332, 33
- Nieto, J.-L. & Bender, R. 1989, *A&A*, 215, 266
- Nolthenius, R. 1993, *ApJS*, 85, 1
- Nomoto, K., Thielemann, F.-K., & Yokoi, K. 1984, *ApJ*, 286, 644
- O'Sullivan, E., Vrtiljek, J. M., & Kempner, J. C. 2005, *ApJ*, 624, L77
- Park, H. S., Lee, M. G., Hwang, H. S., et al. 2010, *ApJ*, 709, 377
- Peletier, R. F., Davies, R. L., Illingworth, G. D., Davis, L. E., & Cawson, M. 1990, *AJ*, 100, 1091
- Posson-Brown, J., Raychaudhury, S., Forman, W., Donnelly, R. H., & Jones, C. 2009, *ApJ*, 695, 1094
- Proctor, R. N. & Sansom, A. E. 2002, *MNRAS*, 333, 517
- PU, S. B., Saglia, R. P., Fabricius, M. H. et al. 2010, *A&A*, 516, A4
- Rampazzo, R., Annibali, F., Bressan, A., et al. 2005, *A&A*, 433, 497
- Rembold, S. B., Pastoriza, M. G., Ducati, J. R., Rubio, M., & Roth, M. 2002, *A&A*, 391, 531
- Rogers, B., Ferreras, I., Pasquali, A., et al. 2010, *MNRAS*, 405, 329
- Saglia, R. P., Bender, R. & Dressler, A. 1993, *A&A*, 279, 75

- Saglia, R. P., Fabricius, M., Bender, R., et al. 2010, *A&A*, 509, A61
- Sánchez-Blázquez, P., Forbes, D. A., Strader, J., Brodie, J., & Proctor, R. 2007, *MNRAS*, 377, 759
- Sánchez-Blázquez, P., Gorgas, J., Cardiel, N., & González, J. J. 2006, *A&A*, 457, 809
- Sánchez-Blázquez, P., Jablonka, P., Noll, S., et al. 2009, *A&A*, 499, 47
- Schuberth, Y., Richtler, T., Dirsch, B., et al. 2006, *A&A*, 459, 391
- Somerville, R. S. & Primack, J. R. 1999, *MNRAS*, 310, 1087
- Tantalo, R., Chiosi, C., & Bressan, A. 1998, *A&A*, 333, 419
- Tantalo, R., Chiosi, C., Bressan, A., & Fagotto, F. 1996, *A&A*, 311, 361
- Thielemann, F.-K., Nomoto, K., & Hashimoto, M.-A. 1996, *ApJ*, 460, 408
- Thomas, D. 1999, *MNRAS*, 306, 655
- Thomas, D., Maraston, C., & Bender, R. 2003, *MNRAS*, 339, 897
- Thomas, D., Maraston, C., Bender, R., & Mendes de Oliveira, C. 2005, *ApJ*, 621, 673
- Thomas, J., Saglia, R. P., Bender, R., et al. 2011, *ArXiv e-prints*
- Tinsley, B. M. 1972, *ApJ*, 178, 319
- Tinsley, B. M. 1980, *Fundamentals of Cosmic Physics*, 5, 287
- Tonry, J. L., Dressler, A., Blakeslee, J. P., et al. 2001, *ApJ*, 546, 681
- Tortora, C., Romeo, A. D., Napolitano, N. R., et al. 2011, *MNRAS*, 411, 627
- Trager, S. C., Faber, S. M., Worthey, G., & González, J. J. 2000, *AJ*, 119, 1645
- Trager, S. C., Worthey, G., Faber, S. M., Burstein, D., & González, J. J. 1998, *ApJS*, 116, 1
- Vazdekis, A. 1999, *ApJ*, 513, 224
- Weijmans, A., Cappellari, M., Bacon, R., et al. 2009, *MNRAS*, 398, 561
- White, S. D. M. 1980, *MNRAS*, 191, 1P
- White, S. D. M. & Frenk, C. S. 1991, *ApJ*, 379, 52
- White, S. D. M. & Rees, M. J. 1978, *MNRAS*, 183, 341
- Worthey, G., Faber, S. M., González, J. J., & Burstein, D. 1994, *ApJS*, 94, 687
- Ziegler, B. L. & Bender, R. 1997, *MNRAS*, 291, 527

6 APPENDIX

Table 2 The full table of measured stellar kinematics as a function of distance from the center (positive: Southeast, negative: Northwest for the position angle of 150°; and positive: Northeast, negative: Southwest for the position angle of 60°)

Galaxy Name	PA (deg)	R (")	V (km/s)	$\pm dV$ (km/s)	σ (km/s)	$\pm d\sigma$ (km/s)	H_3	$\pm dH_3$	H_4	$\pm dH_4$	S/N
NGC4636	150	-13.17	-9.18	± 3.36	199.4	± 4.11	0.019	± 0.015	0.014	± 0.015	121.4
NGC4636	150	-11.77	3.97	± 2.27	205.2	± 2.87	-0.007	± 0.010	0.028	± 0.010	185.3
NGC4636	150	-10.60	2.26	± 2.92	201.6	± 3.64	0.011	± 0.013	0.021	± 0.013	141.2
NGC4636	150	-9.66	1.18	± 2.55	195.3	± 3.07	-0.010	± 0.012	0.007	± 0.012	156.8
NGC4636	150	-8.72	-1.21	± 2.64	202.8	± 3.13	-0.010	± 0.012	0.003	± 0.012	157.7
NGC4636	150	-7.78	-0.25	± 2.66	205.1	± 3.20	-0.004	± 0.012	0.007	± 0.012	157.9
NGC4636	150	-6.84	-0.67	± 2.27	200.0	± 2.79	0.010	± 0.010	0.016	± 0.010	180.2
NGC4636	150	-5.90	-2.00	± 2.40	200.2	± 2.91	0.000	± 0.011	0.010	± 0.011	170.7
NGC4636	150	-5.21	-7.68	± 2.39	200.9	± 2.72	0.007	± 0.011	-0.014	± 0.011	172.5
NGC4636	150	-4.74	-5.64	± 2.75	201.4	± 3.29	0.009	± 0.012	0.006	± 0.012	150.1
NGC4636	150	-4.27	-1.67	± 2.48	204.2	± 2.91	0.000	± 0.011	-0.003	± 0.011	168.5
NGC4636	150	-3.80	-0.92	± 2.41	206.6	± 2.67	-0.014	± 0.011	-0.025	± 0.011	175.5
NGC4636	150	-3.33	-0.78	± 1.99	203.4	± 2.25	-0.003	± 0.009	-0.019	± 0.009	208.9
NGC4636	150	-2.86	0.47	± 2.28	203.3	± 2.70	-0.011	± 0.010	0.000	± 0.010	182.7
NGC4636	150	-2.39	-1.07	± 2.03	209.9	± 2.43	-0.012	± 0.009	0.006	± 0.009	212.0
NGC4636	150	-1.92	-1.35	± 1.93	217.7	± 2.25	0.002	± 0.008	-0.005	± 0.008	231.5
NGC4636	150	-1.45	-0.03	± 1.91	220.0	± 2.17	-0.006	± 0.008	-0.014	± 0.008	236.2
NGC4636	150	-0.98	-2.39	± 1.96	221.5	± 2.31	-0.019	± 0.008	-0.001	± 0.008	231.3
NGC4636	150	-0.51	-2.28	± 2.01	222.5	± 2.41	-0.015	± 0.008	0.007	± 0.008	227.3
NGC4636	150	-0.04	-2.14	± 2.08	225.6	± 2.42	0.002	± 0.008	-0.005	± 0.008	222.5
NGC4636	150	0.44	-0.68	± 1.90	219.1	± 2.08	-0.004	± 0.008	-0.031	± 0.008	235.6
NGC4636	150	0.91	-3.11	± 1.88	216.5	± 2.18	-0.002	± 0.008	-0.007	± 0.008	235.7
NGC4636	150	1.38	-2.54	± 1.98	213.3	± 2.41	0.004	± 0.008	0.012	± 0.008	220.5
NGC4636	150	1.85	-2.33	± 1.99	211.4	± 2.40	-0.002	± 0.009	0.008	± 0.009	217.4
NGC4636	150	2.32	-5.90	± 2.28	209.1	± 2.79	0.007	± 0.010	0.015	± 0.010	188.0
NGC4636	150	2.79	-4.76	± 2.23	210.2	± 2.70	0.015	± 0.010	0.010	± 0.010	192.9
NGC4636	150	3.26	1.75	± 2.59	208.6	± 3.09	-0.003	± 0.011	0.004	± 0.011	164.9
NGC4636	150	3.73	1.93	± 2.24	203.2	± 2.68	-0.005	± 0.010	0.005	± 0.010	185.7

Table 2 Continued

Galaxy Name	PA (deg)	R (")	V (km/s)	\pm dV (km/s)	σ (km/s)	\pm d σ (km/s)	H_3	\pm d H_3	H_4	\pm d H_4	S/N
NGC4636	150	4.20	0.42	\pm 2.21	198.8	\pm 2.49	0.003	\pm 0.010	-0.020	\pm 0.010	183.9
NGC4636	150	4.67	-1.36	\pm 2.54	196.4	\pm 2.84	0.011	\pm 0.012	-0.021	\pm 0.012	158.4
NGC4636	150	5.14	-4.15	\pm 2.72	201.7	\pm 3.35	0.006	\pm 0.012	0.018	\pm 0.012	152.2
NGC4636	150	5.83	-0.15	\pm 2.01	203.7	\pm 2.45	-0.009	\pm 0.009	0.013	\pm 0.009	207.3
NGC4636	150	6.77	-9.65	\pm 2.14	211.7	\pm 2.54	0.010	\pm 0.009	0.002	\pm 0.009	202.3
NGC4636	150	7.71	-4.19	\pm 2.37	206.3	\pm 2.85	-0.001	\pm 0.010	0.006	\pm 0.010	178.1
NGC4636	150	8.65	1.46	\pm 2.73	201.5	\pm 3.52	-0.008	\pm 0.012	0.037	\pm 0.012	151.3
NGC4636	150	9.59	4.50	\pm 2.46	207.4	\pm 3.04	0.021	\pm 0.011	0.018	\pm 0.011	172.5
NGC4636	150	10.76	6.03	\pm 2.50	195.1	\pm 2.97	0.020	\pm 0.012	0.002	\pm 0.012	159.6
NGC4636	150	12.17	-3.08	\pm 2.84	198.2	\pm 3.63	0.044	\pm 0.013	0.033	\pm 0.013	142.9
NGC4636	150	13.58	0.00	\pm 3.22	214.5	\pm 3.87	-0.010	\pm 0.014	0.006	\pm 0.014	136.3
NGC4636	150	15.22	-1.65	\pm 2.95	214.3	\pm 3.42	0.002	\pm 0.012	-0.007	\pm 0.012	149.0
NGC4636	150	17.10	-3.33	\pm 3.58	210.7	\pm 4.32	0.050	\pm 0.015	0.008	\pm 0.015	120.6
NGC4636	150	18.98	-0.47	\pm 3.98	216.8	\pm 4.56	0.046	\pm 0.017	-0.012	\pm 0.017	111.6
NGC4636	150	21.09	2.07	\pm 3.21	204.6	\pm 3.44	0.033	\pm 0.014	-0.038	\pm 0.014	130.4
NGC4636	150	23.44	3.28	\pm 3.34	198.5	\pm 4.03	0.081	\pm 0.015	0.008	\pm 0.015	121.7
NGC4636	150	26.02	0.60	\pm 4.12	214.4	\pm 5.30	0.037	\pm 0.017	0.035	\pm 0.017	106.5
NGC4636	150	29.07	9.97	\pm 3.61	215.5	\pm 4.38	0.019	\pm 0.015	0.011	\pm 0.015	122.3
NGC4636	150	32.59	-5.76	\pm 3.63	209.7	\pm 4.57	0.022	\pm 0.016	0.026	\pm 0.016	118.4
NGC4636	150	36.58	-3.04	\pm 4.25	219.8	\pm 5.31	0.012	\pm 0.018	0.023	\pm 0.018	105.9
NGC4636	150	41.04	4.61	\pm 4.10	225.8	\pm 4.61	0.031	\pm 0.016	-0.019	\pm 0.016	112.9
NGC4636	150	46.20	1.35	\pm 4.96	214.4	\pm 5.22	0.059	\pm 0.021	-0.044	\pm 0.021	88.5
NGC4636	150	52.07	7.14	\pm 5.81	229.5	\pm 6.10	0.050	\pm 0.023	-0.045	\pm 0.023	80.9
NGC4636	150	58.63	-3.40	\pm 4.45	194.6	\pm 3.06	0.112	\pm 0.021	-0.167	\pm 0.021	89.6
NGC4636	150	66.15	-10.48	\pm 4.84	194.2	\pm 4.73	0.107	\pm 0.023	-0.069	\pm 0.023	82.2
NGC4636	150	74.81	-3.40	\pm 6.26	204.3	\pm 4.83	0.121	\pm 0.028	-0.139	\pm 0.028	66.9
NGC4636	150	84.90	-18.95	\pm 5.63	204.1	\pm 6.18	0.14	\pm 0.025	-0.029	\pm 0.025	74.3
NGC4636	150	96.40	-73.35	\pm 4.50	190.8	\pm 5.91	0.161	\pm 0.027	0.044	\pm 0.027	68.6
NGC4636	150	109.70	-21.30	\pm 7.34	191.2	\pm 4.34	0.153	\pm 0.035	-0.073	\pm 0.035	53.4
NGC4636	150	126.20	-99.93	\pm 7.01	147.3	\pm 8.52	0.168	\pm 0.043	0.011	\pm 0.043	43.0
NGC4636	150	137.18	-80.99	\pm 14.87	138.3	\pm 26.35	0.149	\pm 0.098	0.133	\pm 0.098	39.1
NGC4636	60	-5.29	28.13	\pm 3.76	169.7	\pm 4.53	-0.050	\pm 0.020	0.008	\pm 0.020	102.9
NGC4636	60	-4.13	9.01	\pm 4.19	188.8	\pm 4.57	-0.008	\pm 0.020	-0.030	\pm 0.020	102.8
NGC4636	60	-3.19	15.98	\pm 4.05	185.4	\pm 4.62	-0.035	\pm 0.020	-0.014	\pm 0.020	104.3
NGC4636	60	-2.25	10.58	\pm 3.88	190.7	\pm 4.45	0.027	\pm 0.019	-0.012	\pm 0.019	111.9
NGC4636	60	-1.31	1.93	\pm 3.64	205.9	\pm 3.89	0.036	\pm 0.016	-0.038	\pm 0.016	129.1
NGC4636	60	-0.61	-0.57	\pm 3.66	212.1	\pm 3.88	-0.013	\pm 0.016	-0.041	\pm 0.016	132.2
NGC4636	60	-0.14	1.11	\pm 3.61	202.9	\pm 3.77	-0.002	\pm 0.016	-0.047	\pm 0.016	128.3
NGC4636	60	0.33	-7.47	\pm 3.83	214.5	\pm 4.18	0.016	\pm 0.016	-0.031	\pm 0.016	127.5
NGC4636	60	0.80	-3.68	\pm 3.89	208.0	\pm 4.74	-0.010	\pm 0.017	0.012	\pm 0.017	121.8
NGC4636	60	1.49	-3.72	\pm 4.08	193.4	\pm 4.39	0.062	\pm 0.019	-0.036	\pm 0.019	108.0
NGC4636	60	2.43	-4.08	\pm 3.89	159.3	\pm 2.40	0.080	\pm 0.022	-0.191	\pm 0.022	93.4
NGC4636	60	3.37	0.00	\pm 3.58	180.2	\pm 4.12	-0.006	\pm 0.018	-0.011	\pm 0.018	114.6
NGC4636	60	4.31	13.04	\pm 4.68	189.7	\pm 5.49	-0.020	\pm 0.022	-0.003	\pm 0.022	92.3
NGC4636	60	5.47	2.68	\pm 3.41	150.9	\pm 3.29	0.024	\pm 0.021	-0.074	\pm 0.021	100.8
NGC4636	60	7.10	-4.08	\pm 3.49	168.6	\pm 4.00	-0.049	\pm 0.019	-0.012	\pm 0.019	110.1
NGC4636	60	9.20	14.11	\pm 3.74	174.5	\pm 4.30	-0.049	\pm 0.020	-0.011	\pm 0.020	106.2
NGC4636	60	11.77	8.18	\pm 3.86	168.2	\pm 4.59	-0.065	\pm 0.021	0.003	\pm 0.021	99.3
NGC4636	60	15.03	16.04	\pm 3.92	136.0	\pm 4.68	-0.044	\pm 0.026	0.005	\pm 0.026	90.3
NGC4636	60	19.46	5.39	\pm 3.56	149.7	\pm 4.44	-0.070	\pm 0.022	0.022	\pm 0.022	98.4
NGC4636	60	25.71	17.65	\pm 4.58	164.2	\pm 4.58	-0.126	\pm 0.025	-0.061	\pm 0.025	81.7
NGC4636	60	34.90	19.90	\pm 6.52	138.7	\pm 6.76	-0.027	\pm 0.043	-0.049	\pm 0.043	50.6
NGC4636	60	49.04	56.54	\pm 10.23	129.6	\pm 6.04	-0.138	\pm 0.072	-0.137	\pm 0.072	35.8
NGC4636	60	71.14	45.24	\pm 13.98	112.3	\pm 8.26	-0.104	\pm 0.113	-0.125	\pm 0.113	24.7
NGC4636	60	101.22	13.33	\pm 19.39	111.5	\pm 11.46	-0.168	\pm 0.158	-0.201	\pm 0.158	16.6

Table 3 The full table of measured Lick/IDS as a function of distance from the center (positive: east, negative: west) for the different position angles.

Galaxy Name	PA (deg)	R (")	Mgb±dMgb (Å)	Fe5015±dFe5015 (Å)	Fe5270±dFe5270 (Å)	Fe5335±dFe5335 (Å)	Fe5406±dFe5406 (Å)	Hβ±dHβ (Å)
N4636	150	-13.17	4.262±0.039	6.434±0.081	2.374±0.048	2.284±0.062	1.557±0.045	1.869±0.033
N4636	150	-11.77	4.341±0.026	4.515±0.055	2.478±0.031	2.375±0.040	1.577±0.030	1.880±0.022
N4636	150	-10.60	4.454±0.034	5.493±0.070	2.458±0.041	2.396±0.053	1.570±0.040	1.162±0.029
N4636	150	-9.66	4.445±0.030	5.497±0.062	2.562±0.037	2.436±0.047	1.606±0.035	1.702±0.026
N4636	150	-8.72	4.494±0.030	5.601±0.062	2.480±0.037	2.328±0.047	1.718±0.035	1.643±0.025
N4636	150	-7.78	4.597±0.030	5.520±0.062	2.514±0.037	2.529±0.047	1.655±0.036	1.494±0.025
N4636	150	-6.84	4.671±0.026	5.466±0.054	2.645±0.032	2.618±0.041	1.657±0.031	1.480±0.022
N4636	150	-5.90	4.752±0.028	5.532±0.057	2.632±0.034	2.517±0.043	1.766±0.033	1.425±0.024
N4636	150	-5.21	4.854±0.028	5.625±0.056	2.636±0.033	2.494±0.043	1.803±0.032	1.357±0.023
N4636	150	-4.74	4.811±0.032	5.573±0.065	2.712±0.038	2.565±0.050	1.705±0.037	1.393±0.027
N4636	150	-4.27	4.819±0.028	5.599±0.058	2.752±0.034	2.603±0.044	1.681±0.033	1.435±0.024
N4636	150	-3.80	4.898±0.027	5.644±0.056	2.804±0.033	2.730±0.043	1.769±0.032	1.368±0.023
N4636	150	-3.33	4.916±0.023	5.618±0.047	2.762±0.028	2.767±0.036	1.766±0.027	1.239±0.019
N4636	150	-2.86	4.957±0.026	5.702±0.053	2.712±0.031	2.726±0.041	1.742±0.031	1.208±0.022
N4636	150	-2.39	5.027±0.023	5.766±0.046	2.678±0.027	2.694±0.035	1.736±0.027	1.245±0.019
N4636	150	-1.92	5.099±0.021	5.708±0.043	2.795±0.025	2.769±0.033	1.770±0.025	1.221±0.017
N4636	150	-1.45	5.111±0.020	5.623±0.042	2.709±0.025	2.800±0.032	1.764±0.024	1.220±0.017
N4636	150	-0.98	5.125±0.021	5.640±0.043	2.680±0.025	2.811±0.033	1.780±0.025	1.273±0.018
N4636	150	-0.51	5.098±0.021	5.755±0.044	2.706±0.026	2.818±0.034	1.813±0.026	1.351±0.018
N4636	150	-0.04	5.083±0.022	6.045±0.044	2.759±0.026	2.841±0.035	1.811±0.026	1.400±0.018
N4636	150	0.44	5.008±0.020	6.095±0.042	2.774±0.025	2.811±0.032	1.816±0.024	1.449±0.017
N4636	150	0.91	4.957±0.020	6.140±0.042	2.794±0.025	2.827±0.032	1.795±0.024	1.498±0.017
N4636	150	1.38	4.950±0.022	6.113±0.045	2.803±0.026	2.792±0.034	1.762±0.026	1.553±0.018
N4636	150	1.85	4.964±0.022	5.986±0.046	2.759±0.027	2.818±0.035	1.755±0.026	1.571±0.018
N4636	150	2.32	4.958±0.025	5.866±0.053	2.719±0.031	2.796±0.040	1.756±0.030	1.528±0.022
N4636	150	2.79	4.950±0.025	5.835±0.051	2.712±0.030	2.750±0.039	1.816±0.029	1.453±0.021
N4636	150	3.26	4.919±0.029	5.722±0.059	2.671±0.035	2.697±0.045	1.868±0.034	1.488±0.024
N4636	150	3.73	4.876±0.026	5.716±0.052	2.634±0.031	2.756±0.040	1.755±0.030	1.592±0.022
N4636	150	4.20	4.814±0.026	5.797±0.053	2.656±0.031	2.668±0.040	1.685±0.030	1.683±0.022
N4636	150	4.67	4.741±0.030	5.791±0.061	2.570±0.036	2.555±0.046	1.654±0.035	1.685±0.025
N4636	150	5.14	4.669±0.031	5.849±0.065	2.674±0.038	2.668±0.049	1.688±0.037	1.759±0.026
N4636	150	5.83	4.650±0.023	5.973±0.047	2.688±0.028	2.567±0.036	1.661±0.027	1.957±0.019
N4636	150	6.77	4.682±0.024	5.972±0.048	2.686±0.029	2.636±0.037	1.633±0.028	1.789±0.020
N4636	150	7.71	4.580±0.027	5.867±0.056	2.585±0.033	2.572±0.042	1.644±0.032	1.479±0.023
N4636	150	8.65	4.478±0.032	5.693±0.064	2.580±0.038	2.394±0.049	1.582±0.037	1.464±0.027
N4635	150	9.59	4.490±0.028	5.702±0.057	2.600±0.034	2.451±0.044	1.666±0.033	1.494±0.023
N4636	150	10.76	4.279±0.030	5.600±0.061	2.409±0.036	2.239±0.047	1.580±0.035	1.736±0.025
N4636	150	12.17	4.280±0.033	5.802±0.069	2.418±0.041	2.235±0.052	1.561±0.039	1.900±0.028
N4636	150	13.58	4.208±0.036	5.506±0.072	2.560±0.043	2.355±0.056	1.643±0.042	1.844±0.029
N4636	150	15.22	4.137±0.033	5.612±0.066	2.427±0.039	2.300±0.051	1.573±0.038	1.829±0.027
N4636	150	17.10	4.105±0.040	5.803±0.083	2.376±0.049	2.386±0.063	1.485±0.047	1.808±0.033
N4636	150	18.98	4.056±0.044	5.549±0.088	2.335±0.052	2.398±0.068	1.712±0.051	1.857±0.036
N4636	150	21.09	3.880±0.037	5.920±0.075	2.403±0.044	2.227±0.057	1.491±0.043	1.887±0.031
N4636	150	23.44	3.915±0.039	5.522±0.080	2.263±0.048	2.190±0.062	1.570±0.046	1.930±0.033

Table 3 Continued

Galaxy Name	PA (deg)	R (")	Mgb±dMgb (Å)	Fe5015±dFe5015 (Å)	Fe5270±dFe5270 (Å)	Fe5335±dFe5335 (Å)	Fe5406±dFe5406 (Å)	Hβ±dHβ (Å)
N4636	150	26.02	3.884±0.046	5.426±0.093	2.349±0.055	2.199±0.072	1.503±0.054	1.774±0.038
N4636	150	29.07	3.870±0.040	5.451±0.081	2.258±0.049	2.142±0.062	1.492±0.047	1.918±0.033
N4636	150	32.59	3.710±0.041	5.381±0.085	2.398±0.049	2.058±0.064	1.401±0.048	1.987±0.034
N4636	150	36.58	3.620±0.046	4.876±0.096	2.439±0.056	2.056±0.073	1.420±0.055	2.002±0.038
N4636	150	41.04	3.529±0.044	5.369±0.088	2.297±0.052	2.017±0.070	1.478±0.052	1.772±0.036
N4636	150	46.20	3.705±0.055	4.820±0.112	2.319±0.066	1.908±0.087	1.389±0.065	1.554±0.045
N4636	150	52.07	3.483±0.061	5.256±0.124	2.334±0.073	2.086±0.098	1.360±0.073	1.902±0.050
N4636	150	58.63	3.330±0.054	3.758±0.112	2.123±0.065	2.021±0.082	1.268±0.062	1.885±0.045
N4636	150	66.15	3.156±0.059	4.549±0.119	2.281±0.071	1.724±0.090	1.501±0.067	1.746±0.049
N4636	150	74.81	2.927±0.073	4.546±0.150	2.274±0.087	1.910±0.112	1.419±0.084	1.698±0.060
N4636	150	84.90	3.210±0.066	4.632±0.133	2.518±0.079	2.067±0.102	1.435±0.075	2.001±0.054
N4636	150	96.40	2.813±0.071	4.104±0.143	2.383±0.085	1.877±0.107	1.331±0.080	2.043±0.058
N4636	150	109.70	2.452±0.092	4.197±0.183	2.526±0.109	1.631±0.140	1.487±0.103	2.127±0.075
N4636	150	126.20	2.995±0.110	3.588±0.221	2.544±0.132	1.493±0.163	1.265±0.120	2.040±0.093
N4636	150	137.18	3.403±0.243	3.139±0.494	2.376±0.290	2.315±0.357	1.559±0.266	2.171±0.209
N4636	60	-5.290	4.474±0.045	4.803±0.094	2.761±0.055	2.661±0.068	1.681±0.051	2.792±0.039
N4636	60	-4.13	4.720±0.046	4.676±0.096	2.962±0.056	2.600±0.072	1.754±0.053	1.195±0.040
N4636	60	-3.19	4.884±0.045	4.773±0.094	2.936±0.055	2.556±0.070	1.774±0.052	1.117±0.039
N4636	60	-2.25	5.009±0.043	4.928±0.088	2.952±0.052	2.566±0.066	1.892±0.049	1.019±0.037
N4636	60	-1.31	5.019±0.037	5.138±0.079	3.068±0.045	2.719±0.058	1.941±0.043	1.028±0.032
N4636	60	-0.61	5.070±0.036	5.329±0.077	3.101±0.044	2.835±0.057	1.886±0.043	1.053±0.031
N4636	60	-0.14	5.090±0.037	5.196±0.079	3.128±0.045	2.784±0.058	1.870±0.044	0.984±0.032
N4636	60	0.33	5.160±0.038	5.202±0.079	3.075±0.046	2.908±0.060	1.953±0.045	0.941±0.032
N4636	60	0.80	5.028±0.039	5.259±0.082	2.882±0.048	2.791±0.062	1.842±0.046	0.969±0.034
N4636	60	1.49	4.986±0.044	4.869±0.091	3.058±0.053	2.561±0.068	1.817±0.051	1.017±0.038
N4636	60	2.43	4.869±0.049	4.955±0.102	2.790±0.060	2.355±0.074	1.784±0.056	0.953±0.044
N4636	60	3.37	4.922±0.041	5.081±0.086	2.791±0.050	2.534±0.063	1.752±0.047	0.717±0.036
N4636	60	4.31	4.966±0.051	4.781±0.106	2.997±0.063	2.658±0.080	1.803±0.059	0.719±0.044
N4636	60	5.47	4.675±0.046	4.430±0.094	2.798±0.055	2.433±0.068	1.684±0.051	0.946±0.040
N4636	60	7.10	4.527±0.042	5.267±0.087	2.620±0.051	2.266±0.064	1.726±0.048	1.237±0.037
N4636	60	9.20	4.507±0.044	4.910±0.091	2.631±0.054	2.211±0.067	1.632±0.050	1.255±0.038
N4636	60	11.77	4.309±0.047	4.841±0.097	2.349±0.057	2.257±0.072	1.420±0.053	1.716±0.041
N4636	60	15.03	4.223±0.051	4.611±0.104	2.387±0.062	2.343±0.075	1.286±0.056	1.640±0.045
N4636	60	19.46	4.075±0.047	4.622±0.097	2.245±0.057	2.076±0.070	1.461±0.052	1.759±0.041
N4636	60	25.71	3.768±0.057	4.601±0.118	2.205±0.070	2.221±0.086	1.358±0.064	1.443±0.050
N4636	60	34.90	3.186±0.092	4.497±0.188	1.677±0.112	2.255±0.135	1.191±0.100	1.664±0.080
N4636	60	49.04	3.164±0.130	3.836±0.265	1.775±0.157	2.467±0.186	1.159±0.140	1.949±0.113
N4636	60	71.14	2.607±0.188	3.477±0.381	0.940±0.223	2.139±0.266	1.051±0.201	1.427±0.165
N4636	60	101.22	2.575±0.279	3.659±0.568	0.478±0.336	2.835±0.395	1.071±0.296	3.797±0.239